JOURNAL OF COMPUTATIONAL PHYSICS 107, 367–377 (1993)

A Discrete Particle Model for Bubble-Slug Two-Phase Flows*

JOHN A. TRAPP

University of Colorado, Denver, Colorado and Idaho National Engineering Laboratory, Idaho Falls, Idaho 83415

AND

GLEN A. MORTENSEN

Idaho National Engineering Laboratory, EG & G Idaho, Inc., Idaho Falls, Idaho 83415

Received November 20, 1991; revised August 5, 1992

Most two-phase flow models are based on the fully averaged two-fluid concept. This paper describes a new discrete particle model that is intermediate between the numerically intractable local instant description and the fully averaged two-fluid model, thereby providing a more detailed but still tractable description of dynamical two-phase flow phenomena. The new model uses a Lagrangian description for a single dispersed bubble phase and a one-dimensional Eulerian description for a single continuous liquid phase. In contrast to many other particle simulation models, the present model includes compressible phases and large bubbles whose size may be comparable to the computational cell size. The discrete Lagrangian description of the dispersed phase allows the particles to have a distribution of sizes, shapes, etc., thereby capturing the important statistical aspects of dispersed two-phase flow. In contrast to the two-fluid models, the discrete particle model allows the use of more mechanistic models for dispersed phase coalescence and breakup, wakes, etc., thereby allowing the dynamic prediction of flow regime evolution and transitions without the use of flow regime maps inherent in two-fluid models. Numerical simulations for two test problems are presented. Agreement with experimental data is generally satisfactory. Extensions of the model to heat transfer and to two discrete and two continuous phases will be described elsewhere.

I. INTRODUCTION

The modeling and numerical simulation of two-phase flow continues to pose complex and challenging problems. Descriptions based on the local instantaneous Navier–Stokes equations with internal interfaces are clearly intractable in all but the simplest cases. Most current two-phase flow models are based upon the averaged two-fluid concept. This paper describes a one-dimensional model based on a multiphase description that is intermediate between the numerically intractable local instant description and the fully averaged two-fluid model. Dispersed phases are modelled using Lagrangian descriptions for the particles that are embedded within the Eulerian description for the continuous phases. This approach: (1) permits the statistical features of the dispersed phase to be modelled directly, (2) permits the dynamic prediction of flow regime evolution without the explicit use of flow regime maps, and (3) avoids the numerical diffusion associated with Eulerian implementations of multi-field descriptions. Similar models have previously been successfully used to model fuel sprays [1–6]. Our extension to two-phase flow presents additional challenges related to void fraction coupling between compressible phases and bubbles that are no longer small compared to computational cell sizes.

In its present form, the model is limited to a single dispersed phase (bubbles or drops) in a single continuous phase (liquid or gas), and this is the form described in the present paper. The present description is also limited to isothermal flow without heat transfer. Extensions to heat transfer and a second discrete and continuous phase are in progress and will be reported elsewhere.

A computer code, DISCON, has been written to implement this model. Shown in Fig. 1 is a section of a pipe with a simulated dispersed bubbly flow. As is evident in the graphic, spherical bubbles, elliptical bubbles, spherical cap bubbles, and extended cylindrical bubbles are generated as the simulation progresses.

The basic concept of the model is to describe the motion of the dispersed phase using a Lagrangian description. The main motivation is to develop a more mechanistic description of the dispersed phase allowing for distributions of bubble sizes and their interactions. This in turn leads to the dynamic prediction of flow regimes. However, in order for the continuous phase and the discrete phase to interact, it is necessary to relate the two descriptions. This interaction

* Work supported by the U.S. Department of Energy, Assistant Secretary for Conservation and Renewable Energy, under DOE Field Office, Contract DE-AC07-76ID01570.

0021-9991/93 $5.00

FIG. 1. Simulation of bubbly flow using the DISCON computer code.

takes place through three mechanisms: (1) phase coupling, because each phase occupies a volume not available to the other phase (volume fraction coupling), (2) interface drag between the phases (momentum coupling), and (3) coalescence and breakup of the dispersed phase bubbles. The first mechanism proved the most difficult to implement numerically.

The paper is organized as follows. Section II describes the discrete phase Lagrangian model equations for the mechanical case and Section III describes the continuous phase Eulerian model equations for this case. Section IV describes the phase coupling models, Section V contains a summary of the basic equations, Section VI describes the semi-implicit solution scheme, Section VII contains two illustrative simulation and data comparisons, and Section VIII presents some concluding remarks.

II. DISCRETE PHASE LAGRANGIAN MODEL EQUATIONS

The mass and momentum equations for each particle (bubble) are based on the average properties of that particle. Because each particle has its own position in space and is individually tracked, the conservation equations are ordinary differential equations governing the time evolution of mass and momentum. Each evolution equation includes appropriate interaction terms with the continuous phase through which the particle is moving.

A. *Discrete Phase Mass Equation*

The conservation equations are written in a partially discretized form showing the time levels of all source terms. Any undifferentiated term without a time level shown is evaluated at the old, nth, time level. All terms that are evaluated at the new time level contain an $n+1$ superscript. In the following, dQ/dt is understood to mean $(Q^{n+1}-Q^n)/\Delta t$. The mass conservation equation for particle p is

$$\frac{d(\rho_p V_p)}{dt}=0, \tag{1}$$

where ρ_p is the average particle density and V_p is the volume of the particle. In the numerical implementation of all the particle equations, the time derivatives of products are expanded into products of derivatives, and first-order forward differences are used with the coefficients evaluated at the old time level. Because the description of each particle is Lagrangian, the particle density and volume are functions of time only.

B. *Discrete Phase Momentum Equation*

The momentum balance for particle p is

$$\rho_p V_p \frac{du_p}{dt}=\rho_p V_p g - V_p \frac{\partial \bar{P}}{\partial x}-F_p, \tag{2}$$

where u_p is the velocity of particle p and g is the acceleration of gravity. The second term is the interface force due to the mean pressure gradient about the particle. The third term, F_p, is the sum of the interface drag force and the added mass force,

$$F_p=f_p(u_p^{n+1}-\bar{u}_p)+C_a\langle\rho\rangle_p V_p\left[\frac{du_p}{dt}-\langle a\rangle_p\right], \tag{3}$$

where $f_p=(0.5\langle\rho\rangle_p C_d A_p|u_p-\bar{u}_p|)$ is the interface drag coefficient, $\langle\rho\rangle_p$ is the average continuous phase density at the location of the particle, C_d is the drag coefficient, A_p is the equivalent frontal area of the particle, $\bar{u}_p$ is the average far field continuous phase velocity at the location of the particle, C_a is the added mass coefficient, and $\langle a\rangle_p$ is the average continuous phase acceleration at the location of the particle. The particle velocity is evaluated implicitly in

the interface drag term, which removes the need for a small time step due to the large values of the interface drag coefficient, f_p.

C. *Discrete Phase Kinematic Position Equation*

A final equation to advance the particle position, x_p, is needed in this Lagrangian description. It is

$$\frac{dx_p}{dt} = \frac{1}{2}(u_p + u_p^{n+1}). \tag{4}$$

Modifications of Eq. (4) to include simple turbulence effects are described later. These modifications incorporate the fact that the particles are three-dimensional, and therefore, we use two additional kinematic position equations to track the particle in the other two dimensions. However, our model does not include any interaction terms between the continuous phase and the discrete phase in these two perpendicular directions. We also use the three-dimensionality of the particle in the coalescence model to compute the overlap between particles to determine if they should be merged. The coalescence model is described in detail later.

Equations (1)–(4) are solved for each particle. Simulations have been made with the number of particles ranging from one to over 1000.

III. CONTINUOUS PHASE EULERIAN MODEL EQUATIONS

The continuous phase equations for the mechanical case are discretized using a staggered Eulerian mesh, shown in Fig. 2. Mass is conserved in each continuity cell, and momentum is conserved in each momentum cell. The edges of continuity cells are called junctions and are at the centers of the momentum cells. The edges of the momentum cells are at the centers of the continuity cells. Discrete values of densities and pressures are located at the centers of the continuity cells, and discrete velocities are located at the centers of the momentum cells. In the finite difference equations, some variables are needed at locations where they are not defined. Averaging and/or upstream differencing techniques are used to compute these values.

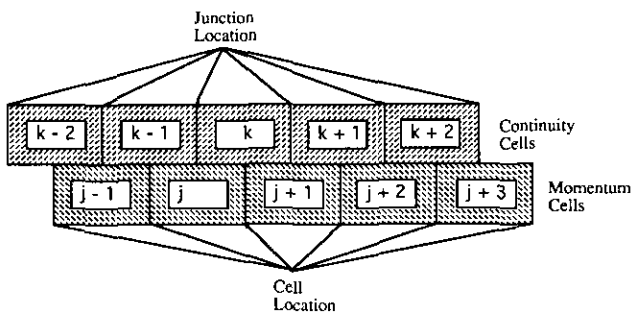

FIG. 2. Continuity and momentum cell locations for the staggered Eulerian grid.

A. *Continuous Phase Mass Equation*

The continuous phase mass balance for volume, V_k, is

$$\frac{\partial(\alpha_k \rho_k V_k)}{\partial t} + A(\alpha_{j+1}\rho_{j+1}u_{j+1}^{n+1} - \alpha_j \rho_j u_j^{n+1}) = 0, \tag{5}$$

where α_k is the continuous phase volume fraction of the control volume, ρ_k is the average phasic density in cell k, V_k is the volume of control volume k, and A is the cross-sectional flow area, which is assumed to be constant. The average continuous phase velocity at junction j is u_j. The variable α is defined in Section IV.A in terms of the particle volume, V_p, and particle location, x_p. In Eq. (5), the second and third terms on the left-hand side represent the flux of mass out of and into cell k. As in the particle equations, the time derivatives are expanded and first-order forward time differences are used with the coefficients evaluated at the old time level. The spatial terms are differenced in a numerically conservative manner.

To prevent a convective instability due to centered flux terms, the fluxed densities in Eq. (5) are differenced using upstream values (donored) if the velocity is not zero. Because the particles are tracked in a Lagrangian manner, there are no instabilities associated with α, and the fluxed volume fractions are not donored.

B. *Continuous Phase Momentum Equation*

The continuous phase momentum equation is

$$\alpha_j \rho_j V_j \left(\frac{\partial u_j}{\partial t} + u_j \frac{\partial u}{\partial x}\right) = -V_j \alpha_j \frac{\partial P^{n+1}}{\partial x} + \alpha_j V_j \rho_j g - F_w u^{n+1} + \sum_{p=1}^{N} \eta_{jp} F_p, \tag{6}$$

where V_j is the momentum cell volume, P is the pressure, F_w is the wall drag coefficient, and η_{jp} is the fraction of particle p in momentum cell j. The variable, η_{jp}, will be explicitly defined in Section IV.A in terms of the particle volumes. Consistency between the particle and the continuous phase momentum interface terms, F_p, must be satisfied. The continuity cell variables with a j subscript are simple averages of neighboring continuity cell values. The convective acceleration terms are evaluated using a one-sided upwind spatial gradient (i.e., donoring to make the convective terms stable). In order to make this scheme implicit in the terms responsible for sound wave propagation, the pressure gradient in the momentum equation and the velocity in the

mass balance are both evaluated at new time. Hence, this scheme does not have the time step limit based on the sound speed that explicit schemes have.

IV. PHASE COUPLING MODELS

The coupling of the discrete Lagrangian and continuous Eulerian phases proved to be the most difficult part of the modeling and numerical algorithm development. This section describes the coupling models under four headings: (A) volume fraction coupling, (B) momentum transfer coupling, (C) coalescence, and (D) a simple turbulence model.

A. *Volume Fraction Coupling*

In two-phase bubbly flow, the dispersed phase bubbles can become quite large due to coalescence, merging to form extended cylindrical bubbles that have transverse diameters approaching the pipe diameter. For this reason, the volume occupied by the dispersed particles can not be neglected as it frequently is in modeling liquid sprays [1–6].

The volume fraction coupling between the dispersed and continuous phases must be treated carefully. The volume of a particle located at x_p is clearly discrete in space. The volume fraction, α, in the continuous phase equations results from these spatially discrete particle volumes. However, in the continuous phase equations, the volume fraction is a continuous field variable with a spatially smooth distribution, as in the classical two-fluid model.

This dual character of the volume fraction means that some smoothing interpolation must be used when the discrete particle volumes are combined to calculate the continuous phase volume fraction. This has been done in DISCON using an extended particle shape function. This should not be confused with the actual shape of the particle, which is described in Section IV.C. The continuous phase model represents the average phase properties over a region of space comparable to the cell length, Δx. Therefore, in order to smooth out this particle-induced continuous phase volume variation, the particle volume is distributed over an arbitrary length. In the present code, this length is set to the Eulerian cell length, Δx. The code has also run successfully with this arbitrary length set to two or three particle diameters. Because the particle locations are Lagrangian, this smoothing does not introduce any artificial diffusion of the volume fraction. It is simply an interpolation of the volume occupied by the discrete particles onto the continuous field volume fraction, which is itself an average value over the cell.

The cross-sectional area occupied by an extended particle at position x and time t is given by $A_p(x, t)$. It will be convenient when we extend the particle's length to partition the cross-sectional area into the product of two terms, the particle's volume, $V_p(t)$, and the particle's shape, $\eta_p(x, t)$. Since, the integral of the cross-sectional area occupied by a particle, $A_p(x, t)$, over its length is equal to the particle's volume, $V_p(t)$, the integral of the particle's shape over the same length must be unity. We also require that the shape function not change as the particle propagates down the pipe, i.e., the (x, t) dependence of the shape function is a function of the relative distance, q_p, from the particle's position, $\eta_p(x, t) = \eta_p(q_p) = \eta_p(x - x_p(t))$, where $x_p(t)$ is the position of the particle. Thus, we have

$$A_p(x, t) = V_p(t)\, \eta_p(x - x_p(t)). \tag{7}$$

If we integrate η_p with respect to x over cell k, we obtain the fraction of the particle that is located in cell k,

$$\eta_{kp}(t) = \int_{\text{cell}\,k} \{\eta(x - x_p(t))\}\, dx. \tag{8}$$

A parallel definition integrating over the length of junction j gives the fraction of the particle that is located in junction cell j, $\eta_{jp}(t)$. If the entire particle is in cell k, then η_{kp} is equal to unity, or if an entire particle is in junction cell j, the η_{jp} is equal to unity.

The integral of Eq. (7) over one Eulerian cell divided by the volume of the cell gives the particle volume fraction in cell k, α_{kp},

$$\alpha_{kp}(t) = \left[\frac{V_p(t)}{V_k}\right] \int_{\text{cell}\,k} \{\eta(x - x_p(t))\}\, dx = \left[\frac{V_p(t)\, \eta_{kp}(t)}{V_k}\right]. \tag{9}$$

The time derivative of α_k appears in the mass conservation equation, Eq. (5). Since

$$\alpha_k = 1 - \sum_{p=1}^{N} \alpha_{kp}, \tag{10}$$

we need the time derivative of the bubble volume fraction, α_{kp}. Differentiating Eq. (9) with respect to time gives

$$\frac{d\alpha_{kp}(t)}{dt} = \left[\frac{\eta_{kp}(t)}{V_k}\right]\left[\frac{dV_p(t)}{dt}\right] + \left[\frac{V_p(t)}{V_k}\right] \int_{\text{cell}\,k} \left\{\frac{d\eta(q_p)}{dq} \frac{\partial[x - x_p(t)]}{\partial t}\right\} dx. \tag{11}$$

Making use of the fact that the time derivative of $x_p(t)$ is the bubble velocity, $u_p(t)$, and that the derivative of q with respect to x is one, we have

$$\frac{d\alpha_{kp}(t)}{dt} = \left[\frac{\eta_{kp}(t)}{V_k}\right]\left[\frac{dV_p(t)}{dt}\right] - \left[\frac{V_p(t)\, u_p(t)}{V_k}\right] \int_{\text{cell}\,k} \left\{\frac{d\eta(q_p)}{dq}\right\} dq. \tag{12}$$

The integral can be written as the difference of the "out" minus the "in" values of η at the two junctions at either end of cell k. Integrating the last term in Eq. (12) and remembering that cell k is bounded by junction j on the left and $j+1$ on the right gives

$$\frac{d\alpha_{kp}(t)}{dt} = \left[\frac{\eta_{kp}(t)}{V_k}\right]\left[\frac{dV_p(t)}{dt}\right] - u_p(t)\left[\frac{V_p(t)}{V_k}\right][\eta(x_{j+1}-x_p(t)) - \eta(x_j - x_p(t))]. \tag{13}$$

Instead of using the point value of η at junction j, the average junction value is used. This results in additional smoothing of the solution as a particle moves from cell to cell. Hence,

$$\frac{d\alpha_{kp}(t)}{dt} = \left[\frac{\eta_{kp}(t)}{V_k}\right]\left[\frac{dV_p(t)}{dt}\right] - u_p(t)\left[\frac{V_p(t)}{V_k}\right]\left[\frac{\eta_{j+1,p}(t)-\eta_{jp}(t)}{\Delta x}\right]. \tag{14}$$

The particle volume fraction in a junction cell is defined in a manner paralleling Eq. (9) and leads to

$$\alpha_{jp}(t) = \left[\frac{V_p(t)}{V_k}\right]\int_{\text{junction } j}\{\eta(x-x_p(t))\}\,dx = \left[\frac{V_p(t)\,\eta_{jp}(t)}{V_k}\right]. \tag{15}$$

Equation (15) gives the relationship between the junction fraction, η_{jp}, and the junction volume fraction due to particle p. Using this in Eq. (14), one obtains the time derivative of the volume fraction due to particle p,

$$\frac{d\alpha_{kp}(t)}{dt} = \left[\frac{\eta_{kp}(t)}{V_k}\right]\left[\frac{dV_p(t)}{dt}\right] - u_p(t)\left[\frac{\alpha_{j+1,p}(t)-\alpha_{jp}(t)}{\Delta x}\right]. \tag{16}$$

This is the expression used in the code development. For a multi-particle system, the right-hand side becomes a sum over all particles.

B. *Momentum Transfer Coupling*

The momentum coupling between the discrete particles and the continuous phase is due to the interface force acting on the surface of the particles. (In Eq. (6), the momentum transfer due to mass transfer has been neglected.) This interface force is modelled in the particle momentum equation by the three terms $f_p(u_p-\bar{u}_p)$, $V_p\partial\bar{P}/\partial x$, and the added mass term.

The first term represents the classical drag force as measured on a particle immersed in a continuous phase. The drag force is formulated in terms of a drag coefficient, C_d, based on the equivalent frontal area. This drag coefficient is obtained from the data correlations of Peebles and Garber [7], Harmathy [8], and Ishii and Chawla [9]. Peebles and Garber give the drag coefficient in the laminar and distorted particle regime. They use a four region formula. Harmathy gives a better formula for Region 4 and adds a fifth formula for the fully turbulent Taylor cap region. The resulting drag coefficients for bubbles are:

$$\begin{aligned} C_d &= 24.0\,(\mathrm{Re})^{-1.0} && \text{(Region 1)},\\ C_d &= 18.7\,(\mathrm{Re})^{-(2/3)} && \text{(Region 2)},\\ C_d &= 0.0275G\,(\mathrm{Re})^4 && \text{(Region 3)},\\ C_d &= 0.488G^{0.25}\,\mathrm{Re} && \text{(Region 4)},\\ C_d &= \tfrac{8}{3} && \text{(Region 5)}. \end{aligned} \tag{17}$$

where Re is the Reynolds number based on the relative velocity, continuous phase properties, and the equivalent particle diameter, and G is the Morton number. The transition from one region to another is carried out in a smooth manner such that C_d is a continuous function of the equivalent particle diameter by switching regions at the point where they give equal values for C_d.

For large bubbles, particles interact with the wall, and the Taylor cap develops a cylindrical tail. Harmathy has summarized the drag data for this flow region and gives for C_d

$$C_d = \left[\frac{1}{\lambda^2}\right]\left[\frac{4r_e}{3R}\right] \qquad \text{(Region 6)}, \tag{18}$$

where r_e is the equivalent bubble radius, R is the pipe radius, and λ depends upon the Eötvos number computed using the pipe radius. The formula used for λ is taken from Stuhmiller, Ferguson, and Meister [10]. A simple exponential transition formula is used in the region between the bubble formulas in Eq. (17) and the cylindrical bubble formula in Eq. (18). The transition formula is that given by Stuhmiller [10].

When using this formulation for a simulation with many bubbles of various sizes, the question arises of what should be used for the continuous phase far field velocity. In the case of a single bubble rising in a uniform fluid, the appropriate continuous phase far field velocity is clear and is easily determined. In the intermediate situations, the appropriate far field reference velocity is not well defined. For cylindrical bubbles that nearly fill the pipe, the

appropriate far field reference velocity is the continuous phase velocity far ahead of or far behind the bubble. Neglecting compressibility effects, this is equivalent to using the mean volumetric flux as the far field reference velocity. At the other extreme of a single small bubble rising in a large tank, the far field velocity is clearly the liquid velocity far from the bubble, which in the limit of vanishing small bubble size is equivalent to the mean volumetric flux.

In the intermediate case, where there are many bubbles of various sizes present in the flow, it is necessary to estimate an equivalent far field velocity for use in the drag correlations. Several papers have recently addressed this problem, see Kowe [11] and Couet [12]. A reasonable model for the interstitial far field velocity that takes into account the added mass of the continuous phase that is displaced with the particles has been developed in these references. This model is applicable to low void fraction dispersed flows. When the bubble number density becomes small, the analysis becomes inappropriate. In DISCON, we consider a full range of bubble number densities and bubble sizes including large cylindrical bubbles filling the pipe. We have chosen to use the mean volumetric flux as the far field reference velocity in all situations. This choice simplified the coding and clearly is appropriate in the limiting cases.

Recalling Eq. (15), one obtains for the volumetric flux at any junction:

$$\bar{u}_j = \alpha_j u_j + \sum_p \alpha_{jp} u_p = \alpha_j u_j + \sum_p \eta_{jp} \frac{V_p}{V_j} u_p. \tag{19}$$

The volumetric far field velocity defined in Eq. (19) is independent of position when the continuous and particle phases are incompressible and there is no mass transfer. In the numerical simulations, it is important to represent this far field velocity with a spatially smooth function independent of the Lagrangian nature of the particles. The velocity in Eq. (19) is consistent with the far field velocities used when the correlations were developed and gives the spatially smooth reference velocity needed in the drag force calculation.

The far field velocity defined above is not the whole story. Each particle can also be influenced by the wake of preceding particles. A trailing particle can be "trapped" in the wake of a leading particle. When a trailing particle, say a bubble rising in a liquid, is in the wake of another bubble, it is rising in a flow field that has a velocity more nearly equal to that of the leading bubble. It rises due to buoyancy in this modified flow field. This is the primary mechanism allowing bubbles to approach and coalesce. This effect is modeled by modifying the far field velocity in Eq. (19) by the wake velocity of leading particles when making the drag calculation.

The velocity in the wake of a solid object has been discussed in several texts, see for example Batchelor [13] and Schlichting [14]. In general, for turbulent flow the wake-induced flow at any position x behind an object can be expressed as

$$u_{\text{wake}} = u_w(x) \exp\left(-\left[\frac{r}{r_w(x)}\right]^2\right), \tag{20}$$

where $u_w(x)$ is the centerline wake velocity and $r_w(x)$ is a scale for the radial distribution of the wake velocity. A standard integral momentum balance gives the relationship between u_w and r_w,

$$\left[\frac{u_w}{u_r}\right]\left[\frac{r_w}{r_p}\right]^2 = \frac{1}{2} C_d, \tag{21}$$

where u_r is the velocity of the wake producing object relative to the fluid, and r_p is the equivalent radius of the particle based upon a spherical shape consistent with the calculation of C_d. Using Eqs. (20) and (21), the velocity at any location behind an object caused by its wake can be found if we know u_w or r_w. Stuhmiller has carried out a preliminary correlation of wake centerline velocity data from several sources and gives a formula for $u_w(x)$,

$$\left[\frac{u_w}{u_r}\right] = \left[a_w + b_w\left(\frac{x}{R_b}\right) + c_w\left(\frac{x}{R_b}\right)^2\right]^{-1}, \tag{22}$$

where $a_w = 0.20$, $b_w = 0.12$, $c_w = 0.01$, and R_b is the actual radius of the particle shape, which is discussed in Subsection C below.

To complete the wake model, the wake velocity of every bubble leading the bubble in question is calculated using the above formulas. The leading bubble that gives the largest wake velocity is used to calculate the modified far field velocity, $\bar{u}_p$, for the trailing bubble. The trailing bubble thus "sees" this modified far field velocity in its drag correlation. It rises in the wake flow field at a rate determined by the balance of drag and buoyancy forces. This is the primary mechanism by which trailing bubbles overtake leading bubbles.

The second momentum coupling term, $V_p \partial \bar{P}/\partial x$, represents the average pressure force on the particle surface due to the mean pressure gradient in the continuous phase. In the present version of DISCON, this effective mean pressure gradient in the continuous phase is modelled using the gravity head and inertial acceleration of the far field continuous phase flow,

$$\frac{\partial \bar{P}}{\partial x} = \langle \rho \rangle_p \left[g - \left(\frac{\partial \bar{u}}{\partial t} + \bar{u} \frac{\partial \bar{u}}{\partial x} \right) \right], \tag{23}$$

where $\langle \rho \rangle_p$ is the continuous phase density at the location of particle p. The first term on the right-hand side combines with the gravitational term in Eq. (2) to give the traditional

buoyancy force. The second term is a correction to include the acceleration of the far-field velocity.

C. *Coalescence*

So far in the development, the actual shape of the dispersed particle has not been a factor in the model. The drag correlations are based upon the frontal area of an equivalent sphere having volume V_p, and the actual shape has not been needed.

In general, bubbles take on a variety of shapes depending upon their size. The sequence of shapes shown in Fig. 3 is generally characterized in increasing volume as spherical, oblate spheroidal, Taylor cap, and cylindrical bubble. We used the simple formulas given by Stuhmiller [10] to characterize each shape. These formulas are based upon the Eötvos number, ε, the particle volume, V_p, and the pipe radius, R.

The Eötvos number is defined as

$$\varepsilon = 4gr_p^2\left[\frac{|\rho - \rho_p|}{\sigma}\right]. \tag{24}$$

These shapes are explicitly used at two places in the model and in all visual output from a DISCON simulation. The actual radius of the particles, R_b, is used in the wake centerline velocity calculation, Eq. (22).

The actual particle radius, R_b, and the actual vertical height of a particle are also used in our simple coalescence model. Two bubbles merge or coalesce if they overlap in the radial and axial directions by more than a certain fraction. This overlap fraction is an input parameter, and in most simulations it is set to zero; i.e., the two bubbles merge when they just touch. When two bubbles are merged, the sum of their masses and momenta are preserved. The merged bubble is placed at the center of mass of the two original bubbles.

D. *A Simple Turbulence Model*

A very simple turbulence model is used to simulate the effect of the fluctuating continuous phase velocity field. The velocity of each particle is assumed to consist of the deterministic velocity component modeled above plus an additive fluctuating component generated by the turbulence present in the continuous phase. The particle positions are then calculated using,

$$\frac{dx_p}{dt} = \frac{1}{2}(u_p + u_p^{n+1}) + u_p', \tag{25}$$

$$\frac{dy_p}{dt} = v_p', \tag{26}$$

$$\frac{dz_p}{dt} = w_p', \tag{27}$$

where u_p', v_p', and w_p' are the velocities generated by the continuous phase turbulence in the x, y, and z directions, respectively. These fluctuating continuous phase velocities are related to the intensity of the turbulent wakes produced by the neighboring particles (wall effects are neglected). A simple random walk process that produces the same fluid parcel dispersion as found in homogeneous turbulence as developed by Tennekes and Lumley [15] is used to estimate the size of u_p', v_p', and w_p', see Stuhmiller [10].

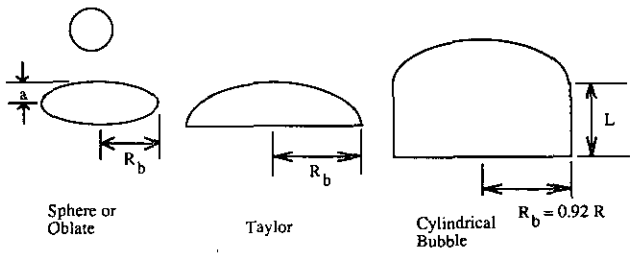

FIG. 3. Calculated bubble shapes.

V. SUMMARY OF BASIC EQUATIONS

For the discrete phase, the basic equations are the mass conservation (1), the momentum balance (2), and the kinematic position equation (4). The continuous field equations for each cell are the mass conservation (5) and the momentum balance (6). The above five equations (per particle, per cell) are the basic equations to be solved for the five new time variables, V_p^{n+1}, u_p^{n+1}, x_p^{n+1}, P_k^{n+1}, u_j^{n+1}. The formulas of Section IV.A, are used to express the volume fraction, α_k, in terms of the particle volume, V_p. The remaining state variables, ρ_p^{n+1} and ρ_k^{n+1}, are functions of the independent state variable, P_k^{n+1}. The present version of DISCON neglects any pressure difference between the phases; therefore, P_k^{n+1} (when interpolated to a particle position) forms an independent state variable for the particle phase. All state relationships in DISCON are linearized during a time step.

An examination of the basic finite difference equations reveals the following:

- They are linear in the new time variables. Hence, each time advancement only requires the solution of a linear system of equations. This is a very complicated linear system due to the mixed Lagrangian and Eulerian features of the equations and the implicit coupling between the phases caused by the time derivatives of α_k in Eq. (5).
- The acoustic terms (i.e., velocities in Eq. (5) and pressure gradient in Eq. (6)) are evaluated implicitly; hence there is no upper limit on the allowable time step size due to acoustic wave propagation.

- The drag term in the particle momentum equation has been evaluated implicitly in u_p. Hence, the short time constant associated with the large drag force on the particle does not lead to a stability restriction of the time step size.

Because of the explicit evaluation of the convective terms in the continuous phase, the time step size is restricted by the material Courant limit. In addition to the material Courant limit stability restriction on Δt, the step size must be chosen to resolve the accuracy of the important physics of any given process.

VI. SOLUTION SCHEME

The solution scheme is a semi-implicit scheme and is outlined below for one time step of the calculation.

At the beginning of each time step, the continuous phase density, acceleration, and volumetric flux are interpolated to obtain local values at each particle location. The shape of the particle is computed and the drag coefficient is determined using Eqs. (17)–(18). The wake velocities at each particle's position due to each of the leading particles is computed using Eqs. (20)–(22). The largest wake velocity is used at each particle position to modify the far field velocity of the particle. Next, coefficients that go into computing the drag and the added mass force on each particle due to the continuous phase fluid are computed using Eq. (3).

Terms that go into the discrete phase momentum equation are now known, and the new time particle velocity is computed using Eq. (2). The new time particle position is computed next from Eq. (4).

The integrated effect of the particles on the continuous phase are computed. These effects are contained in the last term of Eq. (6), which is a summation over all the particles in a momentum control volume.

The continuous phase velocity for each momentum cell is computed using Eq. (6). This velocity is explicit and uses the old time pressure spatial gradient, $P_k^n - P_{k-1}^n$, since we do not know the new time pressure spatial gradient yet. We also compute an influence coefficient, $vdp_j = -\Delta t/(\rho_j \Delta x)$, that can later be multiplied by the spatial gradient of the new time pressure increment, $\Delta P_k^{n+1} - \Delta P_{k-1}^{n+1}$, and added to the explicit velocity, $u_j^{\exp}$, to obtain the new time velocity,

$$u_j^{n+1} = u_j^{\exp} + vdp_j\,[\Delta P_k^{n+1} - \Delta P_{k-1}^{n+1}]. \tag{28}$$

The new time pressure increment, $\Delta P^{n+1} = P^{n+1} - P^n$, is computed using an expanded form of the continuous phase mass equation, Eq. (5),

$$\rho_k V_k \frac{\partial \alpha_k}{\partial t} + \alpha_k V_k \left[\frac{\partial \rho_k}{\partial P}\right] \frac{\partial P_k}{\partial t} + A(\alpha_{j+1}\rho_{j+1}u_{j+1}^{n+1} - \alpha_j \rho_j u_j^{n+1}) = 0, \tag{29}$$

where we have expanded the time derivative into two terms. We replace the two velocities in the mass flux term in this equation with a suitable form of Eq. (28). For the derivative of the volume fraction, $\partial \alpha_k/\partial t$, we use Eq. (16), which brings in a dV_p/dt term, which can be expressed using an expanded form of the particle phase mass equation, Eq. (1),

$$\frac{dV_p}{dt} = -\frac{d\rho_p}{dt} = -\left[\frac{\partial \rho_p}{\partial P}\right]\frac{dP}{dt}. \tag{30}$$

Thus, Eq. (29) becomes a tridiagonal system of equations involving only the pressure increment at cell k, and its adjacent neighboring cells, $k+1$ and $k-1$. This tridiagonal system is solved for the pressure increment in each cell using a simple tridiagonal solver.

With the new time pressure increment known, the new time continuous phase velocity is computed using Eq. (28), and the new time particle volume is computed using Eq. (30).

Using the new time particle volume, the fraction of each particle in cell k, η_{kp}, is computed using Eq. (8), as is the volume fraction of the particle phase in each cell using Eq. (9). The volume fraction of the continuous phase in each cell, α_k, the volumetric flux, and the acceleration terms are also computed at this time.

The new time particle volume allows us to compute a new particle shape prior to checking for the possible merging of two particles. If two particles overlap by some specified fraction, which is input, the two particles are replaced by one particle having a mass equal to the sum of the masses of the two merged particles, a momentum equal to the sum of the momenta of the two merged particles, and volume equal to the sum of the volume of the two merged particles. The new particle is located at the center of mass of the two merged particles. The pressure of the new particle is a mass-weighted average of the pressure of the two merged particles. As a final step, the continuous phase and the particle phase densities are computed from an appropriate state equation.

This concludes one time step of the calculation, and we repeat these steps for the next time step.

VII. SAMPLE TEST PROBLEMS

A. *Comparison with the Crabtree Experiment*

Crabtree and Bridgwater [15] conducted experiments in which they bubbled a gas into the bottom of a large tank containing a viscous liquid and studied the coalescence of a trailing bubble with a leading bubble. They measured the relative motion of vertically aligned bubble pairs, each

having volumes from 10 to 40 cm^3, in a 67% weight solution of sucrose in water. The Reynolds numbers based on bubble diameters were in the range of 40–90. The Crabtree and Bridgwater experimental data were used to check the drag coefficient model for single bubbles and for evaluating the wake velocity model for two successive bubbles.

We simulated their experiment in which a 30 cm^3 bubble was followed by a 25 cm^3 bubble. The rise of the front bubble is essentially unaffected by the trailing bubble, and hence, it has a constant velocity, shown in Fig. 4 as a straight line. Figure 4 also shows a plot of distance versus time for the trailing bubble from the experiment.

Using Eq. (22) with $a_w = 0.20$ as recommended by Stuhmiller, we see from Fig. 4 that the DISCON calculation of the trailing bubble's path deviates from the experimental data as it approaches the leading bubble. With $a_w = 0.20$, we predict that the trailing bubble merges with the front bubble at 0.65 s. However, in the experiment, the time at which the two bubbles merged was closer to 0.8 s. We then modified the centerline wake induced velocity correlation given in Eq. (22) for small separation distances by changing a_w from 0.2 to 0.45. With this change, we obtained almost perfect agreement with the experimental data.

There was a wide scatter in the data points that were used by Stuhmiller in obtaining his original centerline wake velocity correlation. When the modified correlation was plotted over the data, it fit the data as well as Stuhmiller's original correlation. All further simulations were made with $a_w = 0.45$.

B. *Comparison with the Jaycor Experiment*

The simulation model embodied in DISCON is inherently statistical. Because individual particles are tracked, two different simulations with different particle volume and velocity distributions can have similar average values for volume fraction, mean particle velocity, etc. Every run of DISCON is in effect a new experiment when the particle distribution is re-initialized, even if the mean values of the new initialization are identical with the original. Many experiments have been performed on bubbly air–water flows, but almost all report only selected mean values.

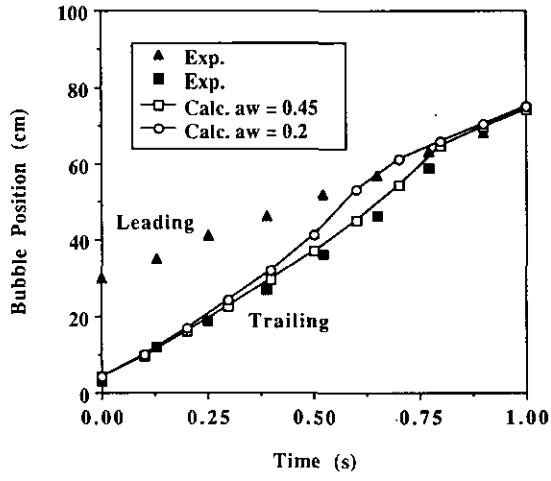

FIG. 4. Position vs time of leading and trailing bubbles in Crabtree simulation.

Stuhmiller from JAYCOR in connection with the development of their BUBBLE code performed an air–water experiment in which fairly detailed statistical data were gathered. In this experiment, air was bubbled up a vertical water-filled pipe, and movies were taken at various axial elevations. At each elevation, the volume and velocity of each passing bubble was measured and recorded. These volumes and velocities were then grouped into a set of bins. For example, all bubbles having velocities between 20 and 22 cm/s were included in the 21 cm/s velocity bin, and all bubbles having volumes between 10 and 12 cm^3 were included in the 11 cm^3 volume bin. Since the raw data was not available, the data from the plots that were published in the EPRI report [10] was digitized and used for our comparisons with the DISCON calculations. The JAYCOR experiment consisted of a 1.27 cm radius circular pipe having a length of 140 cm. The top of the pipe was open, and air was bubbled into the bottom at a flow rate of 22.4 cm^3/s.

The pipe was modeled with DISCON using 17 volumes. A time step of 10 ms was used. With this size time step, a bubble moving at 50 cm/s, which is an upper limit, would take about 16 time steps to move through a cell. Because of the statistical nature of the DISCON model, we used an initial transient period of 100 s, and then gathered numerical data during the following 100 s.

Figure 5 shows a series of frames, spaced every five time steps, of the simulated DISCON calculation in the entire pipe. The first frame is on the left, and frame numbers increase across the page.

The bubble volume data for a typical JAYCOR experiment and the corresponding DISCON simulation are shown in Fig. 6. This figure shows both the mean bubble volume and standard deviation, sigma, at various elevations.

The experimental data show a systematic evolution of the flow regimes with elevation. As the bubbles move up the pipe, they merge causing the mean of the volume distribution to shift to larger and larger values. This is shown in Figs. 5 and 6. As can be seen from Fig. 6, the experimental data show an increasing spread in the bubble volume, i.e., standard deviation, with elevation. Close to the orifice, bubbles are all the same size, while at the higher elevations, some bubbles have merged to give larger bubbles while other bubbles remain at their original size, which results in a larger spread in the bubble volumes.

The numerical simulation shows fairly good agreement

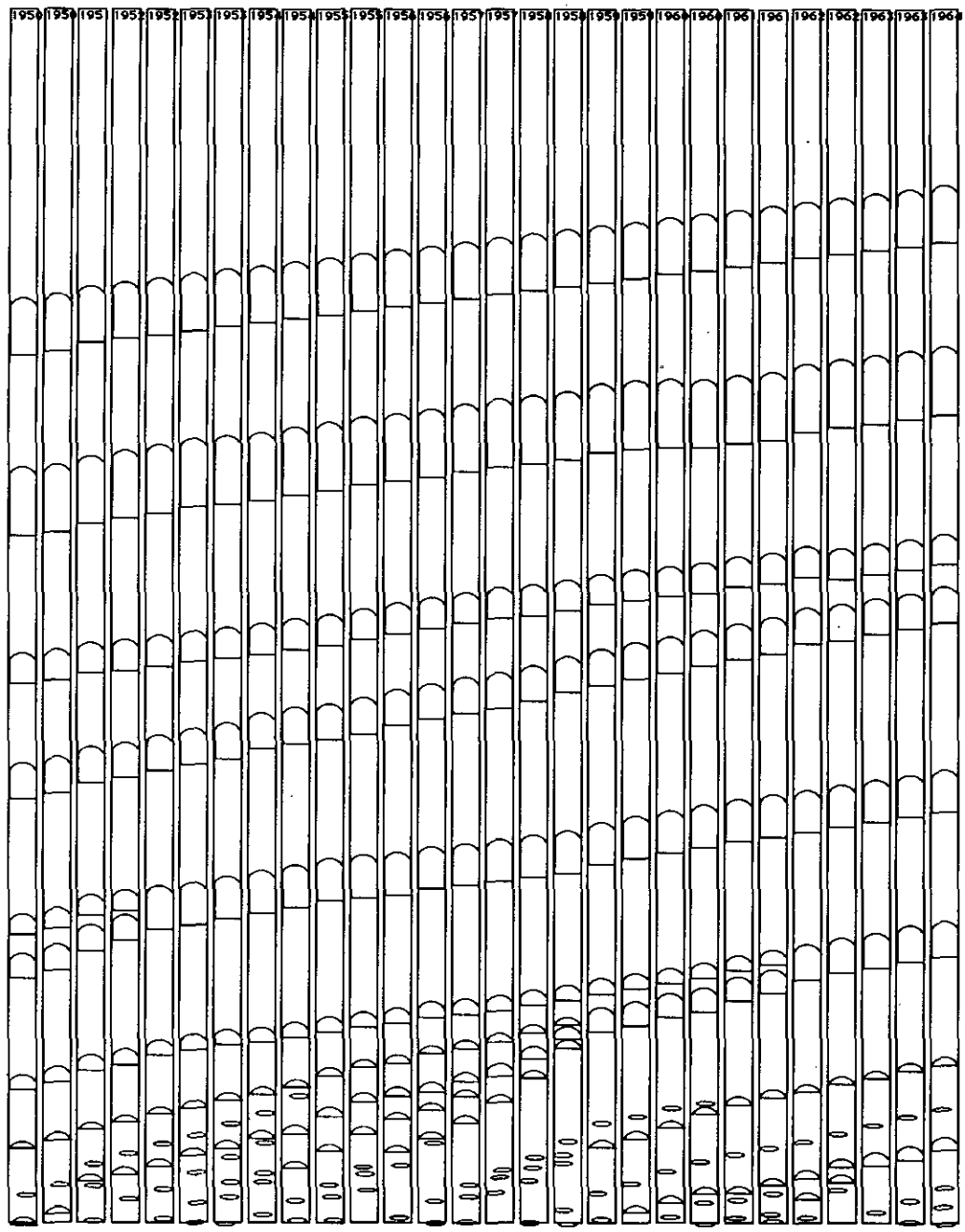

FIG. 5. Calculated bubble shapes near the end of the JAYCOR simulation.

with a slight underprediction of bubble volume at the lower elevations and a slightly higher bubble volume predicted at the higher elevations. There must be more merging occurring in the middle of the pipe in our simulation than in the experiment. It should be noted that DISCON predicted a growth in the standard deviation that parallels the data trend quite accurately given the statistical nature of the data and simulation.

Figure 7 shows the mean and standard deviation of the bubble velocities for both the data from the experiment and the data from the DISCON simulation. The mean bubble velocities are slightly overpredicted by DISCON, which is consistent with the volume data.

It should be noted that while the initial bubbles have an oblate spheroidal shape, they quickly merge to form a Taylor cap shape and then merge again to form cylindrical bubbles. Cylindrical bubbles in this size pipe move at a constant velocity of about 18 cm/s. This singular velocity of a

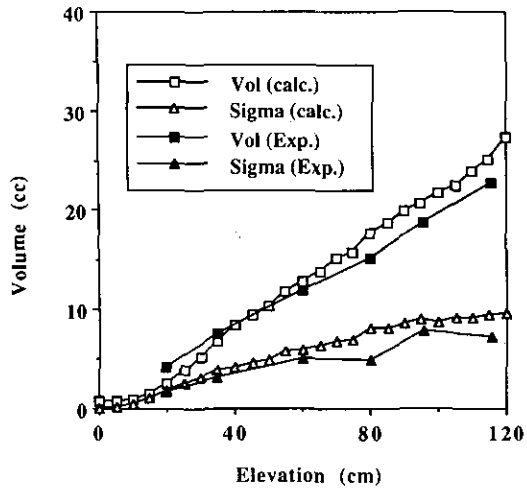

FIG. 6. JAYCOR experiment and DISCON simulation, bubble volume, and sigma vs axial elevation.

cylindrical bubble is evident in the asymptotic character of the mean velocity curves at higher elevations. The mean velocity decreases with increasing axial elevation in the pipe. From this figure, we can see that there are still some smaller bubbles or Taylor caps at the higher elevations of the pipe. The spread in the bubble velocity is almost constant with a slight decrease with elevation because of the constant velocity of the cylindrical bubble. The calculated standard deviation in bubble velocity is somewhat larger than that from the experimental data.

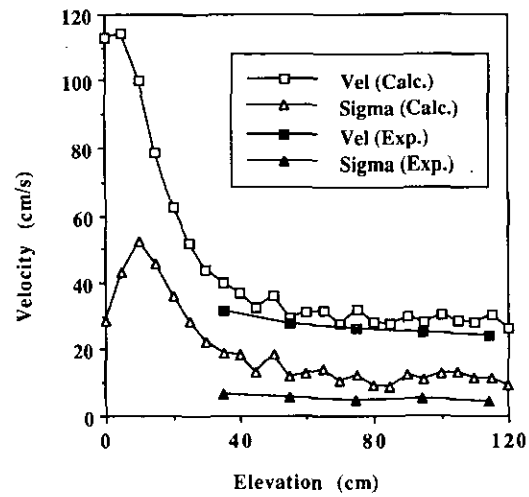

FIG. 7. JAYCOR experiment and DISCON simulation, bubble velocity, and sigma vs axial elevation.

VIII. CONCLUSIONS

The tight coupling of both phases in a two-phase flow requires a discrete particle model that includes implicit volume fraction coupling as well as the traditional momentum interactions. This implicit coupling has been successfully accomplished in the DISCON numerical scheme.

The discrete particle two-phase flow model is able to dynamically predict the evolution of the flow topology as particles merge due to wake effects. Many more simulations must be done, including the effects of bubble generation due to wall heating and the transition from long cylindrical bubbles to annular flow, before a completely mechanistic dynamic evolution of the flow topology can be predicted. Work along these lines is in progress and will be reported elsewhere in due course.

ACKNOWLEDGMENTS

The authors are indebted to V. H. Ransom and J. D. Ramshaw for suggesting the basic approach. We are also indebted to V. H. Mousseau, who developed the initial version of the code, and M. B. Stewart, who compared the results from an earlier version of the code with experimental data.

REFERENCES

1. J. K. Dukowicz, *J. Comput. Phys.* **35**, 229 (1980).
2. J. K. Dukowicz, Los Alamos National Laboratory Report LA-7997-MS, Aug. 1979 (unpublished).
3. P. J. O'Rourke, Ph.D. thesis 1532-T, Princeton University, 1981; Los Alamos National Laboratory Report LA-9069-T, Nov. 1981 (unpublished).
4. P. J. O'Rourke and A. A. Amsden, SAE Paper 872089, 1987 (unpublished).
5. P. J. O'Rourke, *J. Comput. Phys.* **83**, 345 (1989).
6. A. A. Amsden, P. J. O'Rourke, and T. D. Butler, Los Alamos National Laboratory Report LA-11560-MS, 1989 (unpublished).
7. F. N. Peebles and H. J. Garber, *Chem. Eng. Prog.* **49**, 88 (1953).
8. T. Z. Harmathy, *AIChE J.* **6**, 281 (1960).
9. M. Ishii and T. C. Chawla, Argonne National Laboratory Report ANL-79-105, 1979 (unpublished).
10. J. H. Stuhmiller, R. E. Ferguson, and C. A. Meister, Electric Power Research Institute Report NP-6557, Nov. 1989 (unpublished).
11. R. Kowe, J. C. R. Hunt, A. Hunt, B. Couet, and L. J. S. Bradbury, *Int. J. Multiphase Flow* **14**, 587 (1988).
12. B. Couet, P. Brown, and A. Hunt, *Int. J. Multiphase Flow* **17**, 291 (1991).
13. G. K. Batchelor, *An Introduction to Fluid Dynamics* (Cambridge Univ. Press, London, 1967).
14. H. Schlichting, *Boundary Layer Theory* (McGraw-Hill, New York, 1960).
15. H. Tennekes and J. L. Lumley, *A First Course in Turbulence* (MIT Press, Cambridge, MA, 1972).
16. J. R. Crabtree and J. Bridgwater, *Chem. Eng. Sci.* **26**, 839 (1971).